Journal of Materials Chemistry B

ROYAL SOCIETY OF CHEMISTRY

PAPER

View Article Online
View Journal | View Issue

Cite this: J. Mater. Chem. B, 2025, 13, 642

Instant synthesis of nitrogen-doped Ti_3C_2 MXene quantum dots for fluorescence and electrochemical dual-mode detection of norepinephrine with a portable smartphone assay†

Murugesan Chandran, Gayathri Chellasamy, Mekala Veerapandian, Barkavi Dhanasekaran, Saravanan Govindaraju* and Kyusik Yun *

Next-generation 2D materials, such as transition metal carbides and nitrides (MXenes), have received increasing attention owing to their physicochemical properties. In this study, we synthesized highly intense fluorescent materials, nitrogen-doped MXene quantum dots (N-MQDs) using an easy and less time-consuming microwave-assisted method. These N-MQDs are spherical, fluorescent, and highly sensitive materials, as confirmed by high-resolution transmission electron microscopy, atomic force microscopy, UV-visible, fluorescence, Fourier transform infrared spectroscopy, X-ray diffraction, Raman spectroscopy, zeta potential, and contact angle measurements. The N-MQDs were used as dual probes for the fluorescence and electrochemical sensing of neurotransmitter norepinephrine (NE-0.1 to 500 μM). The sensing strategy is based on the Förster resonance energy transfer acquired by the N-MQDs, leading to fluorescence quenching at 400 nm. A new emission peak at 500 nm with color changes and NE-to-NE quinone conversion in an electrochemical reaction. Fluorescence and electrochemical analyses were revealed using the human serum sample limit of detection (LOD) values of 40 and 33 nM, respectively. For point-of-care analysis, we developed a smartphone-integrated sensor array to calculate intensity changes, and the relative red/green/blue (RGB) values were measured at different concentrations of NE. The synthesized fluorescent probe is a promising candidate for detecting NE in biofluids. It is highly selective toward NE and is suitable for the early diagnosis of neurological diseases.

Received 13th August 2024,
Accepted 17th November 2024

DOI: 10.1039/d4tb01818d

rsc.li/materials-b

1. Introduction

Neurotransmitters (NTs) are chemical messengers essential for human life, and imbalances in these can lead to various diseases, such as epilepsy, Parkinson's disease, Alzheimer's disease, and Huntington's disease, as well as high blood pressure, insomnia, and depression.[1] Noradrenaline, also known as norepinephrine or the "stress hormone," is a key catecholamine secreted by noradrenergic neurons in the central and sympathetic nervous systems.[2] NE plays a significant role in physiological processes, including anxiety, stress, memory, sleep, mood, and attention.[3] The normal range of NE in the human body is 70–1700 pg mL^{-1} (413.8–10 048.7 pmol L^{-1}).[1] Low NE levels are associated with pathologies such as depression, Parkinson's disease, and Alzheimer's disease, whereas high NE levels are indicative of paraganglioma, pheochromocytoma, or neuroendocrine tumors. Therefore, it is necessary to develop a rapid and sensitive method for detecting NE in biological fluids.[2]

To date, several analytical methods have been used to detect NE concentrations in human body fluids, including high-performance liquid chromatography (HPLC)[4,5] gas chromatography,[6] capillary electrophoresis,[7] and colorimetric,[8,9] fluorescence,[10–12] and electrochemical techniques.[13–15] However, HPLC, gas chromatography, and capillary electrophoresis are expensive and complicated, have long analysis times and low sensitivity, and require organic and toxic reagents. Therefore, developing a low-cost, sensitive, fast, and selective detection method for NE is essential for point-of-care analyses. Electrochemical and fluorescence techniques are easy to perform, highly selective, and time-efficient. In recent years, electrochemical detection of biomolecules has gained tremendous attention owing to its high selectivity. NE is an

Department of Bionanotechnology, Gachon University, Gyeonggi-do 13120, Republic of Korea. E-mail: biovijaysaran@gmail.com, ykyusik@gachon.ac.kr

† Electronic supplementary information (ESI) available. See DOI: https://doi.org/10.1039/d4tb01818d

electrochemically active molecule that can be converted into NE quinone *via* a two-electron, two-proton transfer process.[16] We used electrochemical induction for early and robust diagnosis of NE concentration in biological fluids; importantly, these inherent advantages made it possible to commercialize the electrochemical platforms. There are two main types of fluorescence-quenching mechanisms: dynamic and static. Dynamic quenching involves a collisional process in which an excited fluorophore interacts with a quencher molecule. These collisions result in nonradiative energy transfer, thereby reducing the fluorescence intensity. Förster resonance energy transfer (FRET) is a type of dynamic quenching in the energy transfer occurring from the excited state of the donor molecule and is fully based on the classical dipole–dipole interaction between the acceptor and donor distances. By contrast, static quenching involves the formation of a stable complex between the fluorophore and the quencher without the need for collisions.[17] The inner filter effect occurs under dynamic quenching because of the loss of fluorescence intensity caused by light absorption through electron transfer. In recent years, mobile-phone-based biosensing platforms have emerged because of their ubiquity, handiness, and accessibility, and they can also be applied in fluorescence, electrochemical, and colorimetric biosensing.[18]

Over the past decade, quantum dot (QD)-based materials have emerged as superior fluorophores for optical sensing and bioimaging owing to their intense fluorescence activity, good solubility, excellent biocompatibility, high surface area, low cytotoxicity, and enhanced surface grafting. Additionally, various probes, such as graphene QDs, nanoclusters, CdTe QDs, CdTe@SiO_2 QDs, and magnetic nanoparticles, have been developed for NE detection.[12,14,19,20] Similarly, amine group-containing ligands, such as polyethyleneimine (PEI) and ethylenediamine (EDA), have been used in ratiometric fluorescence sensor arrays to detect NE.[11,21] MXenes ($M_{n+1}X_n$, where M is an early transition metal, including V, Ti, Zr, Ta, Nb, Sc, Mo, or Hf, and X is nitrogen or carbon) are novel 2D materials derived from the selective etching of the MAX phase ($M_{n+1}AX_n$). Among these, Ti_3C_2 MXene-derived QDs are ideal candidates for cancer therapy and for enzymatic, optoelectronic, bioimaging, and biosensing applications.[22] Functionalized or capped MXene QDs have been used to achieve enhanced stability, high quantum yield (QY), improved luminescence performance, and specific binding of target molecules.[23] Several studies have been conducted on nonmetallic elements (P, S, and N) doped/codoped into MQDs, which provide increased light absorption, improved electrical properties, low energy losses, and increased lifetimes. Owing to their excellent electrical, magnetic, optical, and structural properties, they can be used in metal ion detection, protein detection, photothermal therapy, immunomodulation, electrocatalysis, photocatalysis, photoelectrocatalysis, batteries, supercapacitors, and optoelectronic devices.[24] To date, hydrothermal, solvothermal, hydrothermal/solvothermal-ultrasound, molten salt, acoustomicrofluidic, direct ultrasound, and microwave-assisted methods have been used for the synthesis of MQDs. However, these methods have disadvantages such as being time-consuming, high-temperature, and low-yield.[25] To overcome these effects, microwave-assisted synthesis routes have been widely used because of their short synthesis time, low cost, cleanliness, low temperature requirements, high QY, and ability to produce uniform shapes and sizes.[26] The microwave-assisted synthesis of Ti_3C_2 MQDs is faster, more efficient, and easier than the hydrothermal method.[22] Furthermore, to the best of our knowledge, smartphone-integrated N-MQD-based electrochemical and fluorometric detection of NE has not yet been reported.

In this study, we developed a dual-sensor array for detecting NE in human serum samples using N-MQDs prepared *via* microwave synthesis. We aimed to develop a highly sensitive and selective fluorescent material using a microwave-assisted method within 5 min, which is an environment-friendly and cost-effective approach. Ti_3C_2 MXene was used to synthesize QDs, and triethylamine acted as both a reductant and a nitrogen dopant. The size, surface charge, and fluorescence of the N-MQDs were confirmed by high-resolution transmission electron microscopy (HR-TEM), atomic force microscopy (AFM), zeta potential, and photoluminescence (PL) analyses, and their interactions with NE were confirmed by X-ray photoelectron spectroscopy (XPS). A novel N-MQD sensor array was developed for the electrochemical and fluorescence detection of NE in the 0.1–500 μM range, both in PBS solution at pH 7.0 and in human serum samples. Additionally, the fluorescence sensing performance was analyzed using smartphone-integrated Android-OS-based image analysis, and the RGB (red, green, and blue) values were measured. We chose human serum samples as the biological medium because NE-related disorders, such as Alzheimer's disease, high blood pressure, ganglia neuroblastoma, paraganglioma, and Parkinson's disease, are more common in older adults and can be detected in serum. Compared to other detection techniques, our proposed framework enables effective detection of NE in biological samples with a dual-mode sensor and supports a smartphone-integrated system. N-MQDs are highly sensitive, selective, and promising candidates for detecting NE in biological samples, making them effective for clinical diagnosis.

2. Experimental methods

2.1 Chemicals

MXene (Ti_3AlC_2), ethylene diamine (EDA), sodium hydroxide (≥98%), potassium hexacyanoferrate(III) $K_3[Fe(CN)_6]$ (99%), potassium hexacyanoferrate(II) trihydrate $K_4[Fe(CN)_6]\cdot 3H_2O$ (98.5–102.0%), potassium chloride (KCl-99.0%), calcium chloride (>97%), sodium chloride (99.0%) DL-norepinephrine hydrochloride (≥97%), dopamine hydrochloride (98%) (−)epinephrine, γ-aminobutyric acid (GABA – ≥99%), glucose (≥99.5%), L-ascorbic acid (99%), phosphate-buffer saline (PBS, pH 7.0), and human serum samples were purchased from Sigma Aldrich (USA). Deionized water obtained using a Millipore Milli-Q system (USA) was used to prepare the solutions.

2.2 Instrumentation

A UV-vis spectrometer (Varian Carry 100) was used to record the absorption spectra. A fluorescence spectrometer (SCINCO FS-2)

equipped with FluoroMaster Plus software and a 150-W continuous-wave xenon arc lamp was used to measure the photoluminescence (PL) of the N-MQDs, and HR-TEM (Tecnai™ G2 F30 Series) was used to measure the microscopic images. AFM (JPK NanoWizard II, bioatomic force microscope, Berlin, Germany) was used to measure the height profile images of the N-MQDs. The JASCO FT/IR 4600 enabled spectrum analysis software was used to measure the Fourier-transformed spectrograph images. A micro-Raman system (He–Ne laser beam at 633 nm, Ramboss 500i) was used to measure the Raman spectra of the N-MQDs. A high-temperature X-ray diffractometer (motorized slit; 3 kW X-ray generator; 2-bounce monochromator) was obtained from Texas, USA, and used for an X-ray diffraction (XRD) analysis. XPS (K-Alpha™+) with an Al-Kα micro-hooked X-ray source from Thermo Scientific Inc, USA, was used to study the elemental identification of the N-MQDs, as well as N-MQDs–NE interaction. A Phoenix 300 contact angle instrument was used to measure the surface hydrophobicity and hydrophilicity of the N-MQDs. A NanoKyo-ZetaPALS (phase analysis light scattering, Brookhaven Instruments) analyzer was used to measure the surface charges of the N-MQDs. A microwave oven was used to synthesize the N-MQDs, and luminescent images of the N-MQDs were obtained using an ATTO ultraviolet (UV-365 nm) transilluminator. A BioLogic Scientific Instrument from France with EC Lab software (sp-350) was used for the electrochemical studies.

2.3 Synthesis of N-MQDs

Firstly, the Ti_3C_2 MXene was synthesized by the previously reported method.[27] The N-MQDs were synthesized using a less time-consuming (5 min) microwave-assisted method. Briefly, 50 mg of MXene powder was added to a 250 mL round-bottom (RB) flask containing 50 mL of distilled water and sonicated for 15 min to obtain a uniform dispersion of MXene. Ethylene diamine (2 mL) was added to the RB flask, sonicated for 5 min, and placed in a microwave reactor for 5 min (800 W, 100 °C). The obtained solution was filtered through a dialysis membrane (2000 kDa, KWCO) for 2 d. Finally, the collected samples were lyophilized for 2 d to obtain N-MQDs powder and stored at 4 °C in a refrigerator for further use.[22]

2.4 Fluorescence detection of NE using N-MQDs

1 mg of N-MQDs was dispersed in 1 mL of DI water and sonicated in 15 min for uniform dispersion. Different concentrations of NE (0.1–500 μM) were prepared, and a 4 mL glass cuvette was used for the fluorescence detection experiment. A solution consisting of 100 μL of N-MQDs and 100 μL of NE solution in 1.8 mL of PBS (pH 7.0) was prepared and mixed well using a pipette. After 5 min of incubation, the fluorescence spectrum was measured. Each measurement was repeated three times to standardize the results. The same protocol was used throughout the experiment. For real sample analyses, human serum samples were diluted 20-fold using PBS solution. The NE solutions were spiked with human serum, and the same protocol was used for the fluorescence detection of NE in real samples.

2.5 Electrochemical detection of NE using N-MQDs

A GCE was polished using a 0.05 μm alumina slurry, then 1 mg of N-MQDs were dispersed in 1 mL of DI water and 20 μL of N-MQDs was mixed with 5% Nafion (10 μL). After 5 min of sonication, 5 μL of Nafion mixed N-MQDs were drop-cast on the GCE surface and dried at 50 °C. The N-MQD-modified GCE was used as the working electrode, a Pt wire was used as the counter electrode, and Ag/AgCl was used as the reference electrode. Cyclic voltammetry (CV) and electrochemical impedance spectroscopy (EIS) were used to measure the 5 mM ferri/ferro solution. Differential pulse voltammetry (DPV) was performed using 2 mL of PBS (10 mM, pH-7) solution. Different concentrations of NE (0.1–500 μM) were used for DPV studies. Similarly, as mentioned above, for a real-world application, the human serum samples were diluted 20-fold and spiked with different concentrations of NE. Each experiment was repeated thrice, and the RSD values and recovery percentages were tabulated.

3. Results and discussion

3.1 Morphological, optical, and analytical studies of N-MQDs and sensing of NE

The morphology, size, and line-profile height of the N-MQDs were characterized using HR-TEM and AFM (Fig. 1). Fig. 1a shows the TEM images of the N-MQDs, which exhibited well-dispersed particles, and the inset image shows a size destruction histogram with a diameter of 4–6 nm. Fig. 1b shows HR-TEM images of the N-MQDs with a sequential lattice fringe spacing of 0.265 nm.[22,28] The less time-consuming microwave-assisted N-MQD synthesis provided a uniform size with spherical morphology and high product purity. The height and morphology of the N-MQDs were also measured using AFM, and the results matched those of the HR-TEM analysis. Fig. 1c shows 2D topographic images of the N-MQDs, which had an average height of 5 nm, and Fig. 1d shows the corresponding 3D images.[28] Both HR-TEM and AFM analyses confirmed that the synthesized N-MQDs were spherical with an average size of 4–6 nm.

Fluorescence spectroscopy was used to analyze the optical properties of N-MQDs (Fig. S1, ESI†). Initially, we performed N-MQD synthesis by varying the time (2, 5, 10, and 15 min) and checked the fluorescence image (inset: images under 365 nm UV light) and fluorescence spectrum analysis, as shown in Fig. S1a (ESI†). Increasing the microwave irradiation time from 2 to 5 min doubled the fluorescence intensity compared to the 2-min reaction. Subsequently, we gradually increased the reaction time to 10 and 15 min; thereafter, no drastic change in the fluorescence intensity was observed and the intensity is not stable in the 10 and 15 min prepared samples. The 2 to 10 min synthesized N-MQDs exhibited an emission wavelength of 400 nm, whereas the 15 min synthesized N-MQD samples

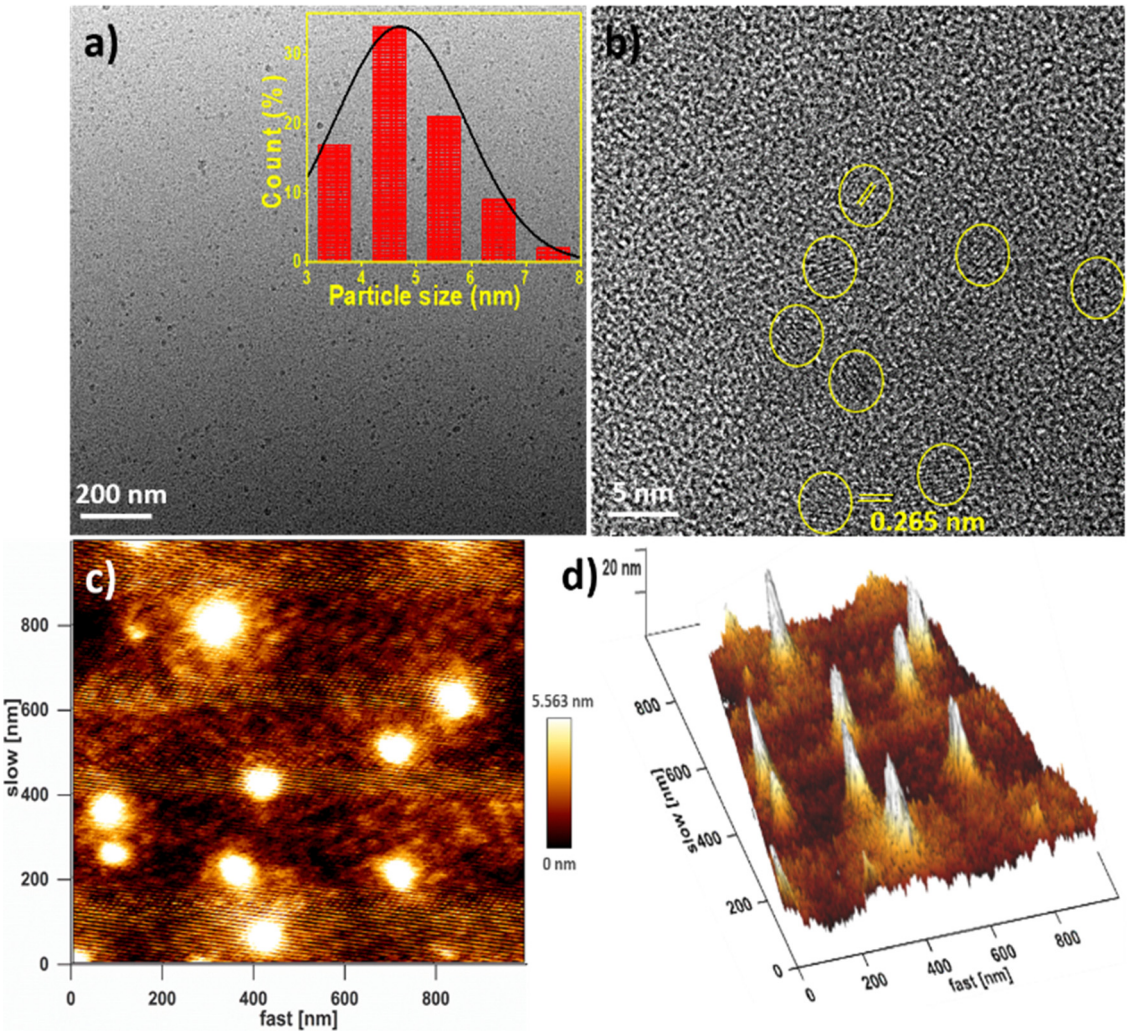

Fig. 1 (a) TEM image of the synthesized N-MQDs (inset: size distribution histogram), (b) HR-TEM image of the N-MQDs, (c) AFM 2D image of the synthesized N-MQDs, and (d) corresponding 3D image.

exhibited an emission peak at 410 nm. Based on this study, we concluded that the 5-min reaction gives the best fluorescence properties, and we also aimed to prepare an intense fluorescent material with a less time-consuming method; therefore, we finalized the 5-min synthesis for our work. Excitation, emission, and excitation-dependent emission spectra were studied to determine the emission wavelengths and maximum intensities of the N-MQDs. As seen in Fig. S1b (ESI†), the N-MQDs exhibit excitation at 330 nm and emission at 400 nm, and the inset figure appears colourless under daylight also with blue fluorescence emission under 365 nm UV light. An excitation-dependent emission spectrum was observed from 300 to 380 nm, as shown in Fig. S1c (ESI†). When the excitation wavelength was increased from 300 to 380 nm, a red shift in the emission wavelength was observed, indicating that the N-MQDs exhibited excitation-dependent PL behavior.[29] Fig. S1d (ESI†) shows the emission spectra of the N-MQDs in PBS solutions with different pH ranges (5–9). A highly intense emission peak was observed at pH 7.0. Thus, the entire experiment was performed at the same pH. Because N-MQD materials are highly stable, with intense fluorescence at neutral pH, they can be used in biological applications.

To further confirm the optical and analytical properties of the as-prepared N-MQDs, the UV-vis, FT-IR, XRD, and Raman spectra are shown in Fig. 2. Fig. 2a and b show the UV-vis and FT-IR spectra before and after the interaction of the NE with the N-MQDs. Fig. 2a shows the absorption peak observed from 290 to 340 nm, which corresponds to the inter-band transition of the N-MQDs. Another broad peak is observed at 400–480 nm.[28,29] The UV-vis spectrum of the 100 μM NE sample showed no peak in this region. However, after interaction with the N-MQDs, a new strong absorption peak appeared at 295 nm. The enhancement of the peaks between 400 and 480 nm, along with the new peak at 295 nm, confirmed a strong interaction between NE and N-MQDs.

In Fig. 2b, the FT-IR spectrum of the N-MQDs shows a broad band at approximately 3303 cm^{-1} corresponding to the OH stretching vibration. The N-MQDs display two strong

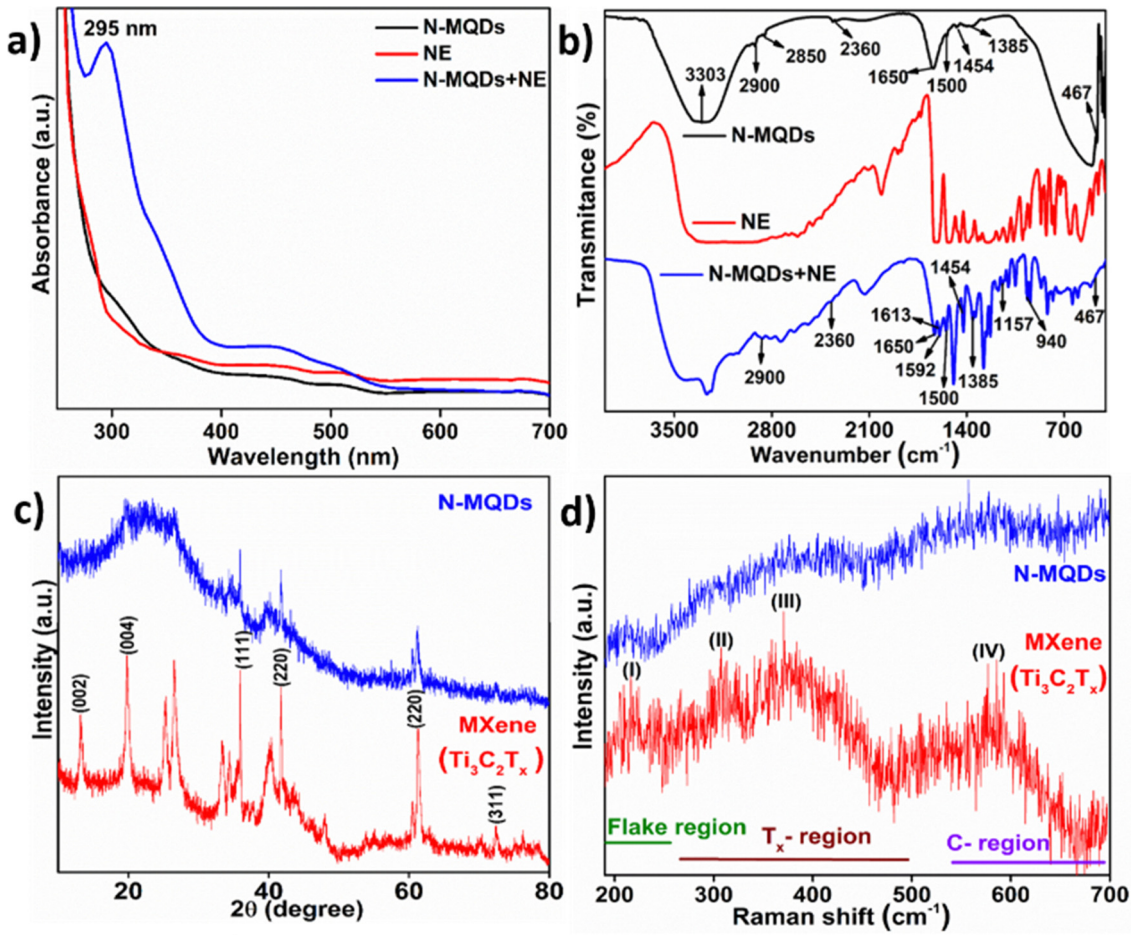

Fig. 2 (a) UV-visible spectrum of N-MQDs, NE, and N-MQDs with NE, (b) IR spectrum of N-MQDs, NE, and N-MQDs with NE, (c) XRD spectrum of MXene and N-MQDs, and (d) Raman spectrum of MXene and N-MQDs.

transmission bands near 2900 and 1500 cm^{-1}, corresponding to the N–H stretching vibration and amide bands, respectively.[28] The peak at 2850 cm^{-1} represents the C–H stretching vibration, while the CO_2 peak appears at approximately 2360 cm^{-1}.[30] The peak at 1650 cm^{-1} corresponds to N–H stretching vibrations, and the peak at 1454 cm^{-1} represents the Ti–O–Ti vibration. The absorption peak at 1358 cm^{-1} is attributed to C–N stretching, and the peak at 467 cm^{-1} corresponds to Ti–C stretching.[31] NE has one NH_2 group, allowing for six types of vibrational modes: symmetric stretching (ν_s), anti-symmetric stretching (ν_{as}), twisting (τ), wagging (ω), rocking (μ), and scissoring (ρ).

NE showed a broad absorption spectrum at 2800–3350 cm^{-1}, attributed to the antisymmetric and symmetric vibrations of the NH and OH groups. The scissoring, rocking, and wagging modes of the NH_2 group are attributed to the ranges 1500–1700, 900–1150, and 825–818 cm^{-1}, respectively. Antisymmetric and symmetric stretching modes of CH_2 were observed in the range of 2700–3000 cm^{-1}, and the C–N stretching vibration appeared at 1095 cm^{-1}.[32,33] C–C skeletal vibrations appeared at 1613 cm^{-1}, while the 1580 cm^{-1} vibration corresponded to C–O. The peak at 1375 cm^{-1} represented CH_2 wagging and twisting vibrations, and the C–H bending vibration appeared at 1075 cm^{-1}. The NE with N-MQDs displayed new peaks at 1592, 1157, and 940 cm^{-1}, corresponding to NH_2^+, C–O stretching vibrations, and C–H out-of-plane bending, respectively.[34] The peak at 1592 cm^{-1} confirms the occurrence of electron transfer between the NE and N-MQDs and the strong interactions between them. To support this, zeta potential analysis was performed (Fig. S2, ESI†). The N-MQDs exhibited a zeta potential value of −10.94 mV, which became 9.04 mV after interacting with NE owing to the NH_2 and OH groups in NE (Fig. S2a and b, ESI†). Contact angle measurements were conducted to assess the wettability of the synthesized N-MQDs, where 10 μL of the sample was drop-cast onto a carbon paper electrode (CPE) and dried in an oven at 50 °C. The pristine CPE electrode showed a contact angle of 104.21° and the N-MQD-modified electrode showed a contact angle of 32.57°, indicating greater hydrophilicity. The synthesized QDs were easily bonded to the analytes and are promising candidates for biosensing applications (Fig. S2c and d, ESI†).

Fig. 2c and d present the XRD and Raman spectra of the MXene and N-MQDs, respectively. XRD was used to determine the crystal structure and phase of the synthesized material. As

shown in the XRD spectrum (Fig. 2c), a scan range of 10–80° was used, and the MXene (Ti_3C_2) showed peaks at 13.05°, 19.5°, 25.4°, 26.5°, 33.4°, 34.4°, 35.8°, 40.1°, 41.7°, 48.2°, 61.2°, and 72.4°, corresponding to the (002), (004), (111), (200), (220), (311), (002), (002), (002), and (002) crystal planes.[35,36] The XRD spectrum of MXene (Ti_3C_2) indicates its crystalline nature, which matches JCPDS no. 52-0875. The scanning electron microscopy (SEM) images further confirmed the removal of Al from the MAX phase. Fig. S3a–c (ESI†) shows the MAX phase images, and the sheet-layered images at different magnifications shown in Fig. S3d–f (ESI†) indicate the removal of Al atoms, further confirming the formation of the MXenes (Ti_3C_2). As mentioned above, the XRD results for the N-MQDs indicated that all the peaks decreased, although minor peaks at 35.8°, 41.7°, and 62.2° were observed. This confirms the successful formation of MQDs. Fig. 2d presents the Raman spectra of $Ti_3C_2T_x$ and N-MQDs, where the vibrations of $Ti_3C_2T_x$ consist of out-of-plane (A_{1g}) and in-plane (E_g) peaks for both the C and Ti atoms. The $Ti_3C_2T_x$ spectrum was divided into three regions: the flake region (I), vibration of the surface functional groups (T_x – II and III), and vibration of carbon (C region – IV). The A_{1g} peaks at 210 (I) cm^{-1} and E_g peaks at 310 (II) and 385 cm^{-1} (III) correspond to the vibrations of the titanium surface groups.[37,38] The E_g peak at 580 cm^{-1} represents the vibrations of carbon atoms, and the A_{1g} and E_g peaks of titanium and carbon correspond to layered MXene ($Ti_3C_2T_x$). After conversion into QDs, the layered A_{1g} and E_g peaks of titanium and carbon were reduced, indicating the successful formation of QDs.[39]

The chemical state, surface composition, and interaction mechanism of the N-MQDs with the NE were investigated using XPS (Fig. 3 and Fig. S4, ESI†). In Fig. 3(ai)–(di) and (aii)–(dii) represent the Ti 2P, C 1s, O 1s, and N 1s spectra of the N-MQDs before and after interaction with the NE, respectively. The XPS survey spectrum confirmed the presence of Ti, C, O, and N in the N-MQDs, with percentages of 8.1%, 62.40%, 27.22%, and 1.51%, respectively (Fig. S4, ESI†). After interaction with the NE, the Ti and C percentages decreased to 2.94% and 51.5%, respectively, and the N and O percentages increased to 12.88% and 32.68%, respectively. The percentage of N increased because of the presence of an amine functional group in the NE. As shown in Fig. 3(ai), the Ti 2P (Ti $2P_{3/2}$ and Ti $2P_{1/2}$) spectrum of the N-MQDs was split into six peaks at 464.3, 463.3, 460.8, 458.4, 456.2, and 454.7 eV corresponding to TiO_2 ($2P_{1/2}$), Ti^{3+} ($2P_{1/2}$), Ti–C ($2P_{1/2}$), TiO_2 ($2P_{3/2}$), Ti^{3+} ($2P_{3/2}$), and

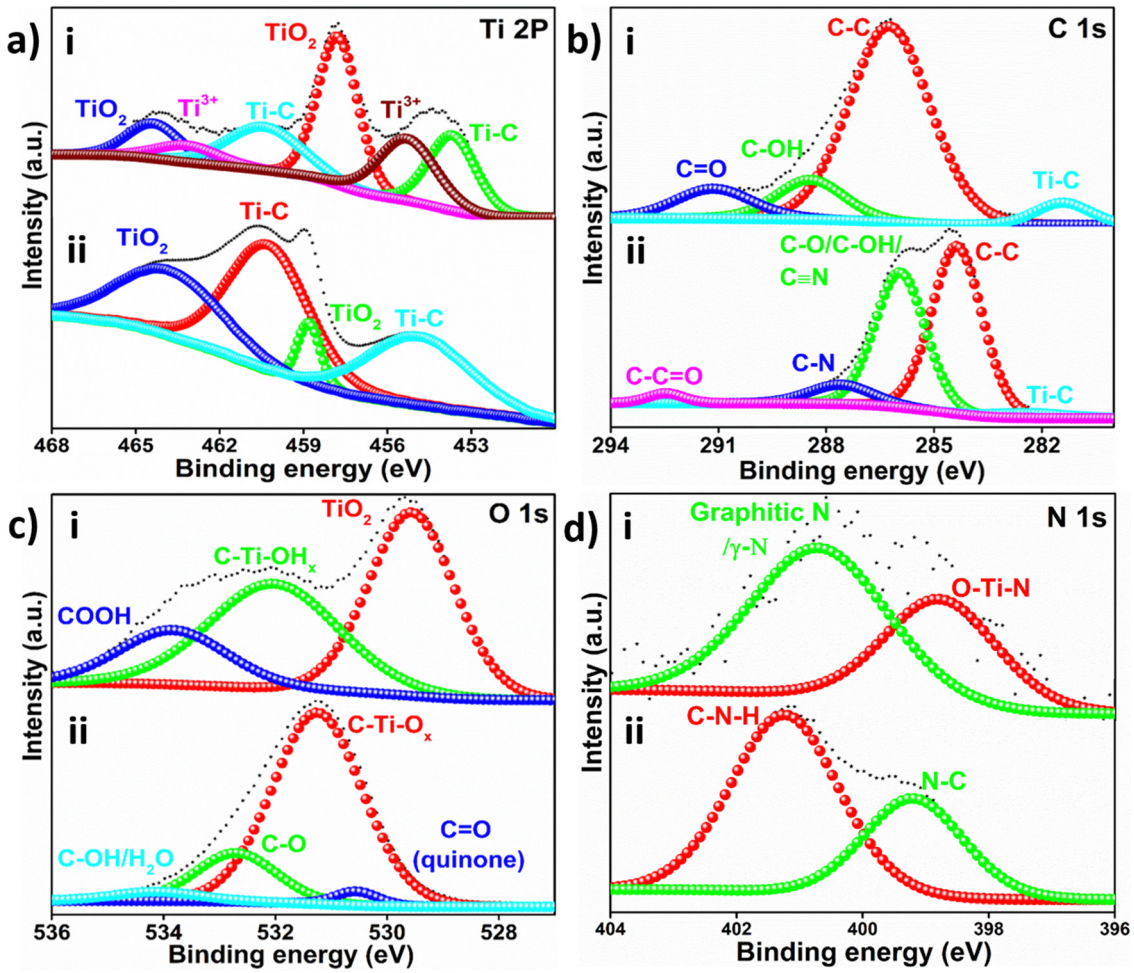

Fig. 3 Figures (ai)–(di) represent the XPS spectrum of N-MQDs and (aii)–(dii) correspond to after interaction of NE with N-MQDs.

Ti–C ($2P_{3/2}$).[40–42] These results indicate the presence of surface functional groups of oxide (–O–) and hydroxyl (–OH) groups. After interacting with NE, Ti–C, and TiO_2 ($2P_{1/2}$ and $2P_{3/2}$) peaks were observed. The Ti–C ($2P_{3/2}$), TiO_2 ($2P_{3/2}$), Ti–C ($2P_{1/2}$), and TiO_2 ($2P_{1/2}$) peaks were observed at 455.0, 458.8, 460.4, and 464.1 eV, respectively (Fig. 3(aii)).[40–42] The C 1s spectrum (Fig. 3(bi)) was split into four spectra, and the peaks at 288.7, 286.9, 284.9, and 281.1 eV corresponded to C═O, C–OH, C–C, and Ti–C, respectively. After interacting with NE, C 1s peaks were observed at 292.4, 287.6, 285.9, 284.3, and 282.3 eV representing C–C═O, nitrogen-bonded carbon, C–O/C–OH, C═N, C–C, and Ti–C, respectively (Fig. 3(bii)).[40,43,44] The peaks at 292.4 and 287.6 eV conformed to the quinone formation and electron transfer that occurred between the NE and N-MQDs.

The O 1s spectra of the N-MQDs (Fig. 3(ci)) showed three peaks: the COOH and C–Ti–O_x peaks were observed at 533.8 and 532.0 eV indicating oxygen–bound carbon atoms and oxygen–bound titanium carbide, respectively.

An intense TiO_2 peak is observed at 529.5 eV representing the formation of titanium oxide. After interaction with NE, a new peak was observed at 530.5 eV representing C═O (quinone), which confirmed the occurrence of electron transfer between the N-MQDs and NE, resulting in NE-to-NE quinone conversion.[45–47] The peaks at 534.2, 532.6, and 531.2 eV are attributed to the formation of C–OH, C–O, and C–TiO_x, respectively (Fig. 3(cii)). In the N 1s spectrum of the N-MQDs, peaks appeared at 400.7 and 398.7 eV, corresponding to graphitic nitrogen (γ-nitrogen) and O–Ti–N, respectively (Fig. 3(di)). Based on the XPS data, we confirmed the successful incorporation of nitrogen atoms into the MQDs; the nitrogen spectrum of the NE with N-MQDs showed two peaks at 401.2 and 399.2 eV corresponding to C–N–H and N–C formation, respectively (Fig. 3(dii)).[48–50] The peak at 401.2 eV corresponds to the amine group of the NE molecule through carbon interactions. The XPS and FT-IR data were consistent, suggesting that the N-MQDs contained hydroxyl and amine functional groups that facilitated the conversion of NE to NE quinone.

3.2. Plausible mechanisms

We propose plausible mechanisms for both the fluorescence and electrochemical detection of NE using the N-MQD sample; the corresponding schematics are shown in Fig. 4. The XPS and FT-IR spectra revealed the presence of hydroxyl and amine functional groups on the N-MQD surfaces. The amine-functionalized MQDs acted as nucleophiles *via* the lone pair of electrons on the nitrogen atom. In addition, NE exhibits two hydroxyl groups on its benzene ring and has remarkable redox properties owing to its excellent ionizability, as well as an amine functional group. The amine group of NE catalyzes the reaction and abstracts the proton from the N-MQDs. The protons from the hydroxyl groups in the NE are abstracted by the oxygen anions of the N-MQDs, eventually generating stable phenoxide anions on the NE surface. The negative charge of the oxygen atom in the NE was delocalized through the benzene ring resonance structure to form the NE quinone structure, as shown in Fig. 4a.[18] Furthermore, the formation of the NE quinone by an electron moving from the N-MQDs to the NE, resulted in quenched PL intensity. Thus, the strong interaction between the 2-amino-1-hydroxyethyl group and the N-MQDs revealed the specificity of the sensor. Similarly, NE is a catechol neurotransmitter; therefore, its oxidation to NE quinone occurs *via* two-electron and two-proton transfer processes. The order of electron and proton transfer is shown in Fig. 4b.[13,51]

3.3 Fluorescence detection of NE

The N-MQD-based fluorescence detection of the NE is shown in Fig. 5. The N-MQDs exhibit an emission peak at 400 nm. When different concentrations of NE (0.1, 0.25, 0.5, 1, 5, 10, 25, 50, 100, 250, 500 μM) were added to the N-MQDs, the fluorescence intensity was significantly quenched by 55% (Fig. 5a). The absorption of light by the sample and electron transfer occurred through FRET, resulting in quenching of the fluorescence intensity.[52] Fluorescence quenching was observed with increasing NE concentrations from 0.1 to 500 μM and 100 μM, a new emission peak at 500 nm because of the conversion of NE to NE quinone.[53] The quenched fluorescence intensity was plotted as a linear function of the initial intensity (F_0/F) *versus* different concentrations of NE (0.1–500 μM) Fig. 5b. The Stern–Volmer equation, $F_0/F = Q\ (1 + K_s)$, was used to analyze the relationship between the quenching efficiency of the N-MQDs

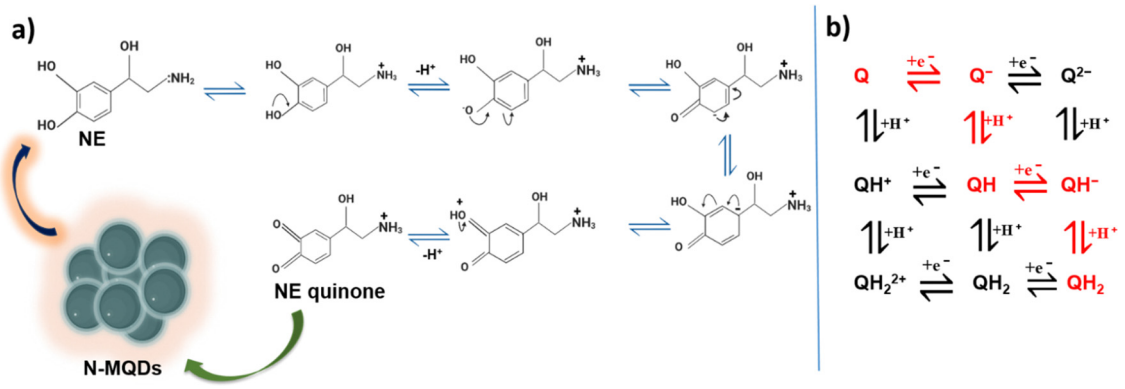

Fig. 4 (a) Scheme representing the possible mechanism for fluorescence quenching of N-MQDs in the presence of NE, and (b) the scheme of squares represents the possible proton and electron transfer sequences of NE.

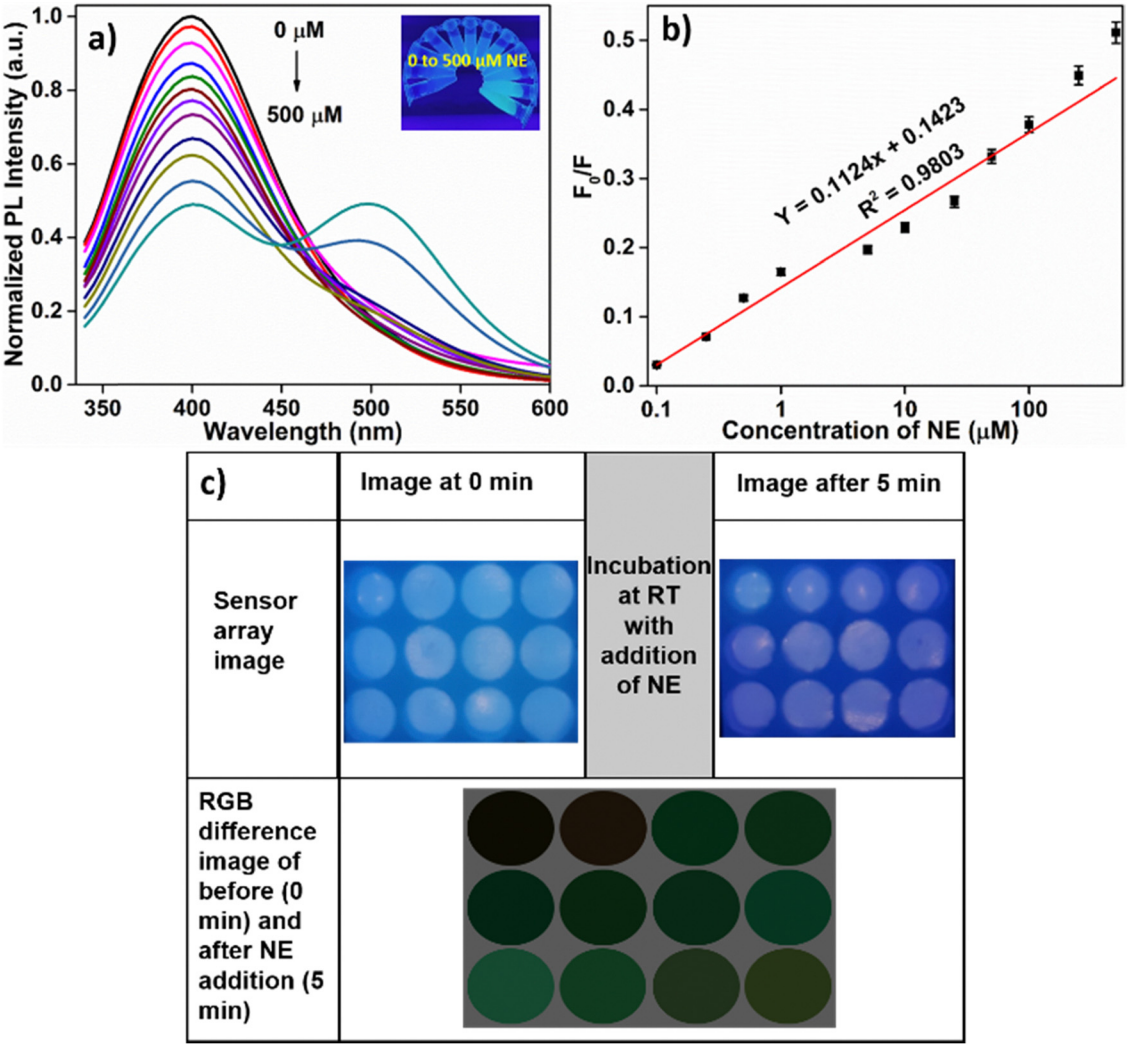

Fig. 5 (a) PL spectrum of N-MQDs with different concentrations of NE from 0 to 500 μM (inset: N-MQDs with different concentrations of NE from 0 to 500 μM samples under 365 nm UV-light), (b) corresponding linear regression plot, (c) RGB difference image of N-MQDs with different concentrations of NE (0.1 to 500 μM) analysis by a smartphone-based color sensor array under UV light. (Each experiment was repeated three times and the standard deviation data were expressed).

and the NE concentration. The LOD was calculated using the formula LOD = $3S/q$, where q is the slope of the calibration curve and S is the standard deviation. Each experiment was repeated three times, and the LOD of 37 nM, R^2 = 0.9803 was observed. Notably, an isobestic point was observed beyond 100 μM of the NE samples. Fig. S5a (ESI†) illustrates the PL spectrum of the N-MQDs and different concentrations of NE, ranging from 500 to 1000 μM. As the concentration of the NE sample increased gradually from 500 μM, the fluorescence intensity at 400 nm decreased, accompanied by the appearance of a new emission peak at 500 nm. The linear relationship between the fluorescence intensity ratio (F_{500}/F_{400}) and NE concentration is shown in Fig. S5b (ESI†), and R^2 = 0.992 was observed. Fig. S5c (ESI†) shows the PL spectra of 250 μM NE, and N-MQDs, and N-MQDs with 0.1 and 250 μM of NE. The N-MQDs exhibited an emission peak at 400 nm, whereas the NE did not exhibit an emission peak in this region. In the case of 0.1 μM NE with N-MQDs, fluorescence quenching accompanied by a color change was observed under UV light. Similarly, for the 250 μM NE with N-MQDs, a 45% fluorescence quenching was noted, and the appearance of a new peak at 500 nm indicated the conversion of NE to NE quinone. The inset image shows the NE, N-MQDs, and N-MQDs with 0.1 and 250 μM of the NE samples under 365 nm UV light. To evaluate the practical applicability and reliability of the developed sensor, a commercial serum sample was diluted 20-fold in PBS. NE samples with selected concentrations (0.1–500 μM) were spiked into the serum sample, and the fluorescence spectrum was recorded (Fig. S6a, ESI†). As the concentration of NE increased, fluorescence quenching was observed without a reduction in sensitivity; a linear regression coefficient of R^2 = 0.9805 and a LOD of 40 nM were observed (Fig. S6b, ESI†). The corresponding recovery percentages and relative standard deviations are presented in Table S1 (ESI†). N-MQDs are potential

candidates for detecting NE without reduction in sensitivity and could be used in real-world applications.

The UV-vis spectrum was used to further confirm the interaction mechanism between NE and N-MQDs, as shown in Fig. S7 (ESI†). Different concentrations of NE (0.1–500 μM) were used, and increasing the concentration of NE in the N-MQD solution altered the color under both visual and UV light (inset image). For the N-MQDs, an absorption peak is observed at 290–340 nm, whereas no peaks are observed for the NE sample in this region. The N-MQDs in the presence of NE exhibited enhanced peaks at 295 and 440 nm. NE possesses a phenolic moiety that can be oxidized in the presence of N-MQDs, and phenol undergoes deprotonation to produce phenolate ions. The ionization of the phenolic moiety facilitates electron transfer from the phenolate ion to the N-MQDs, resulting in a color change. Simultaneously, the phenolate ions undergo structural conversion to semiquinones. The formed semiquinone further converted into NE quinone, which was confirmed by the absorption peak at 295 owing to π–π* transition in the phenyl ring.[54] The inset image shows N-MQDs with different concentrations of NE (0 to 500 μM) sample in daylight and under 365 nm UV light. A smartphone-integrated sensor array was used to perform POC analysis for NE detection, using a step-by-step guide for image capture, as reported in our previous study.[18] The red/green/blue (RGB) values and the relative intensity changes were measured (Fig. 5c). The N-MQDs and different concentrations of NE (0.1–500 μM) were added to the sensor spots and incubated for 5 min. A gel array mobile application was used to analyze the relative RGB changes based on the circle Hough transform algorithm. The smartphone-integrated sensor array extracted the mean, median, and standard deviations of the RGB color changes at 0 and 5 min intervals, and the results were concordant with the UV-visible data upon increasing the concentration of the NE RGB values. A stepwise analysis of the NE samples using the smartphone-based application is shown in Fig. S8 (ESI†).

3.4 Electrochemical sensing of NE

CV and EIS were used to study the electrochemical behavior of the N-MQDs-modified electrode in a 10 mM PBS (pH 7.0) solution containing 5 mM ferri/ferro and 0.1 M KCl (Fig. 6). The bare GCE exhibited redox peaks at 0.248 and 0.334 V, with oxidation currents of 1483 μA cm^{-2} and reduction currents of −1440 μA cm^{-2} (Fig. 6a). By contrast, for the N-MQDs-modified electrode, a potential shift was observed, along with double the oxidation (3104 μA cm^{-2}) and reduction (−2938 μA cm^{-2}) currents, indicating high electrochemical activity of the N-MQD-modified electrode. EIS was used to measure the electron transfer resistance of the N-MQDs; the Nyquist diagram is shown in Fig. 6b, the inserted circuit was used to fit the impedance spectrum, which included four parts: solution resistance (R_s), charge transfer resistance (R_{ct}), parallel composite element (Q), and diffusion resistance (Z_w). The pristine GCE showed a resistance of 940 Ω, suggesting that the electrode had a higher electron transfer resistance. The N-MQDs-modified GCE showed a resistance of approximately 237 Ω. This indicates the low resistance and high electrical conductivity of the synthesized material, which provided excellent active sites for the redox probe.

Similarly, the electrochemical behaviors of the N-MQDs with and without NE were investigated using CV in a 10 mM PBS solution. For the pristine GCE, no noticeable redox peak was observed. By contrast, the N-MQDs-modified electrode exhibited an oxidation peak at 0.36 V, as shown in Fig. S9a (ESI†). After the addition of 250 μM of NE to the electrolyte, oxidation peaks were observed at −0.007 and 0.394 V, while reduction peaks were noted at 0.213 and −0.169 V, respectively, indicating a two-electron and two-proton transfer process (Fig. S9b, ESI†). The detailed mechanism is discussed in Section 3.2 and Fig. 4b. Fig. S9c (ESI†) shows the effect of pH on the oxidation of NE in 10 mM PBS solution using the N-MQD-modified electrode, with pH values ranging from 5 to 9. On increasing the pH, a negative potential shift was observed, and the highest redox current was observed at pH 7.0, after which the redox current decreased. Therefore, the entire experiment was conducted at pH-7.0, and the corresponding current and potential changes are shown in Fig. S9d (ESI†).

To investigate the kinetics of the electrode reaction, a scan rate effect study was performed, as shown in Fig. 6c. CV was conducted using the N-MQD-modified electrode in a 10 mM PBS (pH 7.0) solution at different scan rates ranging from 10 to 100 mV s^{-1}. The corresponding oxidation and reduction peak currents as a function of the scan rate are presented in Fig. 6d. The regression coefficients of the anodic and cathodic peak currents were R^2 = 0.999 and R^2 = 0.998, respectively. Based on these results, we confirmed that the N-MQD-modified electrode underwent a diffusion-controlled reaction. When the scan rate increased from 10 to 100 mV s^{-1}, the diffusion of ions at the electrode–electrolyte interface increased, and both the anodic (I_{pa}) and cathodic (I_{pc}) peak currents increased linearly. The reaction proceeds *via* two-electron and two-proton transfer processes. A peak was observed at 0. 420 V (10 mV s^{-1}), indicating the presence of NE quinone and the completion of the oxidation reaction. A peak was observed at 0.020 V, indicating the presence of the NE semiquinone, which is an intermediate step. The semiquinone (intermediate step) was not stable; therefore, we considered the full reaction step (0.420 V) for the scan-rate effect study. At 10 mV s^{-1}, the anodic peak and cathodic peak potential (ΔV) difference was observed at 0.233 V, denoting the quasi-reversible electrochemical behavior of the developed sensor.[55,56] In addition, the anodic and cathodic peak currents were unequal. The corresponding regression coefficients are expressed as,

$$J = 0.748\nu\ (\text{mV s}^{-1}) + 54.688; \quad R^2 = 0.999 \qquad (1)$$

$$J = 1.071\nu\ (\text{mV s}^{-1}) + 24.850; \quad R^2 = 0.998 \qquad (2)$$

DPV was performed to determine the sensitivity and LOD of the NE sensor using the N-MQD-modified electrode under the optimal conditions, as shown in Fig. 6e. The figure shows a well-defined oxidation peak (0.267 V) for the N-MQD-modified electrode in 10 mM PBS solution. Different concentrations of

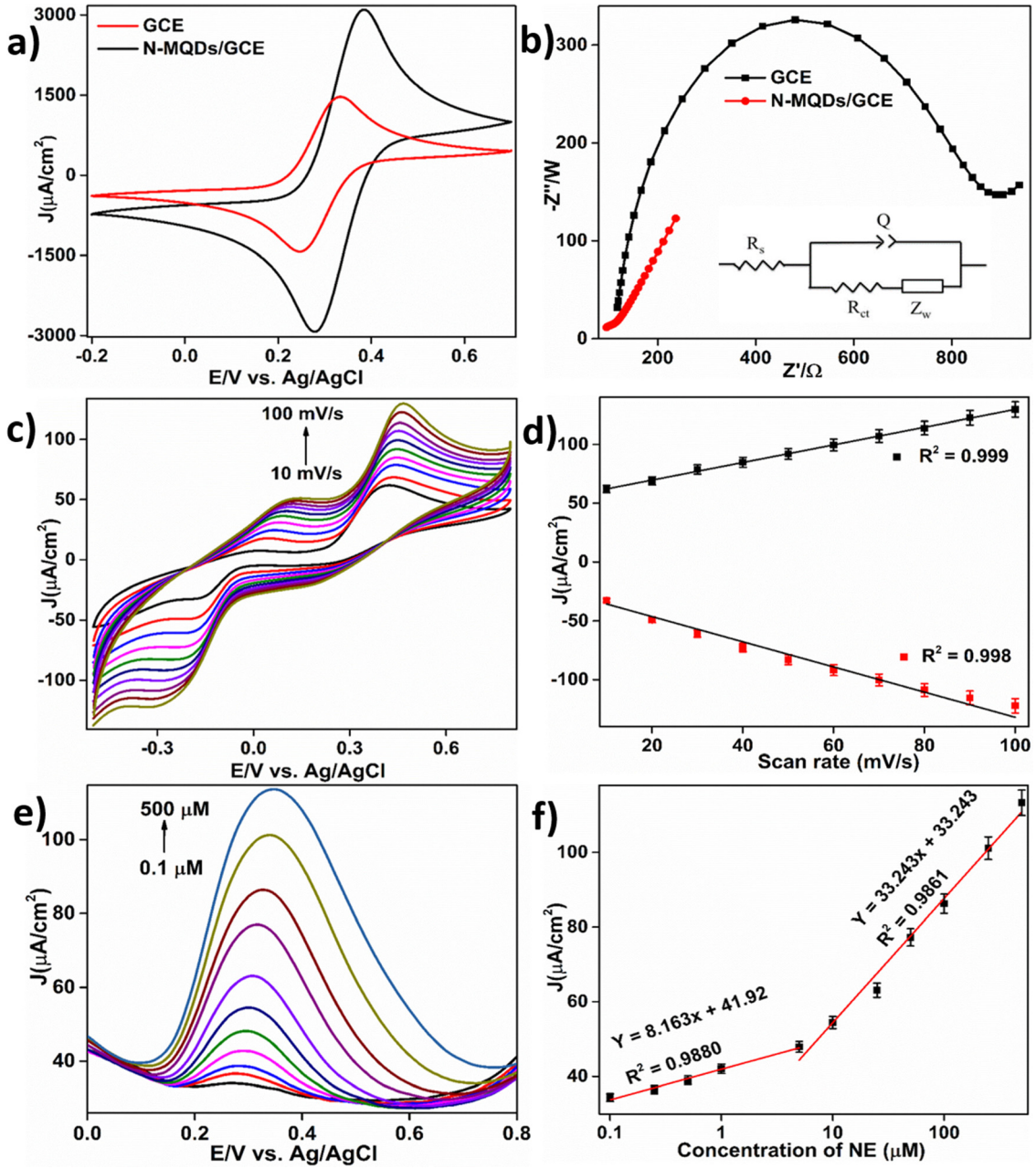

Fig. 6 Electrochemical detection of NE using the N-MQD modified electrode, (a) and (b) are CV and impedance spectrum of the bare GCE and N-MQD modified GCE using 10 mM PBS (pH-7.0) solution containing 5 mM of ferri/ferro with 0.1 M KCl solution, respectively (Fig. b inset: equivalent circuit diagram used for fitting of impedance data), (c) CV of various scan rates from 10 to 100 mV s^{-1} using 10 mM PBS (pH-7.0) solution, (d) corresponding calibration plot, (e) DPV analysis using an N-MQDs modified GCE with different concentrations of NE from 0.1 to 500 μM, and (f) corresponding linear regression plot.

NE (0.1, 0.25, 0.5, 1, 5, 10, 25, 50, 100, 250, 500 μM) were used, and the DPV was recorded between the potentials from 0 to 0.8 V, with a step potential of 0.05 V, an amplitude of 0.025 V, and a scan rate of 50 mV s^{-1}. The fabricated electrodes exhibited excellent electrochemical activity toward NE sensing. When the concentration was increased, a potential shift and an increase in the oxidation current were observed. The reason behind this potential shift may be owing to electrode surface and mass transport effects. The interaction of the NE with the electrode surface can improve its conductivity or modify its adsorption behavior. These changes influence the potential for efficient electron transfer. In addition, increasing the concentration of NE can affect the dynamics of mass transport and the thickness of the diffusion layer because of the greater availability of NE for oxidation. This led to a potential shift toward a more positive direction in the DPV analysis. Fig. 6f shows the corresponding linear graph. The regression coefficient for 0.1–10 μM was R^2 = 0.9880, and that for 10–500 μM was R^2 = 0.9861.

Excellent sensitivity was obtained with a LOD of 54 nM, based on the following equation: LOD = $3S/q$. The N-MQD-modified GCE exhibited excellent catalytic activity for NE detection. For real-world applications, selected concentrations of NE were spiked with a 20-fold diluted human serum sample (Fig. S10a, ESI†). DPV analysis was used for the real sample analysis of NE detection with a potential range of 0–0.8 V, step potential of 0.05 V, and a scan rate of 50 mV s^{-1}. Selected concentrations of NE (0.1–500 μM) were used for real sample analysis. As shown in the figure, a predominant oxidation peak is observed at 0.257 V, and increasing the concentration increases the oxidation peak current. Fig. S10b (ESI†) shows the corresponding linear graph. The regression coefficient for 0.1–10 μM was R^2 = 0.9909 and that for 10–500 μM was R^2 = 0.9791. An LOD of 33 nM was achieved. The recovery percentages and relative standard deviations are listed in Table S2 (ESI†). The N-MQD-modified electrode is a potential candidate for the detection of NE in real samples without a reduction in sensitivity. Table S3 (ESI†) compares the NE detection results using various methods with those of previously reported sensors, highlighting the nanomaterials used for detection, analytical methods, linear range, and LOD.

3.5 Reproducibility and stability

The reproducibility of 10 μM NE detection using the N-MQDs-modified electrode was evaluated with seven individually prepared electrodes by employing DPV in the potential range of 0–0.8 V, as shown in Fig. S11a (ESI†). Predominant oxidation was observed at 0.267 V without reducing the sensitivity and was highly repeatable; therefore, the prepared electrode was highly reproducible for NE detection. Fig. S11b (ESI†) shows the corresponding current response as a bar chart, representing the reproducibility of the proposed sensor. Fig. S11c (ESI†) demonstrates the stability of the developed sensor for NE detection using the N-MQD-modified electrode. The CV was recorded in 50 cycles at potentials between −0.4 and +0.7 V, with a scan rate of 50 mV s^{-1} in 10 mM PBS. This resulted in an RSD decrease of 1.0% in the initial electrochemical current response after 50 cycles. These results demonstrate the consistent stability of the developed sensor and its ability to retain activity for over 50 cycles.[57]

3.6 Specificity of dual-mode NE detection

Interfering compounds exist in the extracellular serum and fluids of the central nervous system, including dopamine (DA),

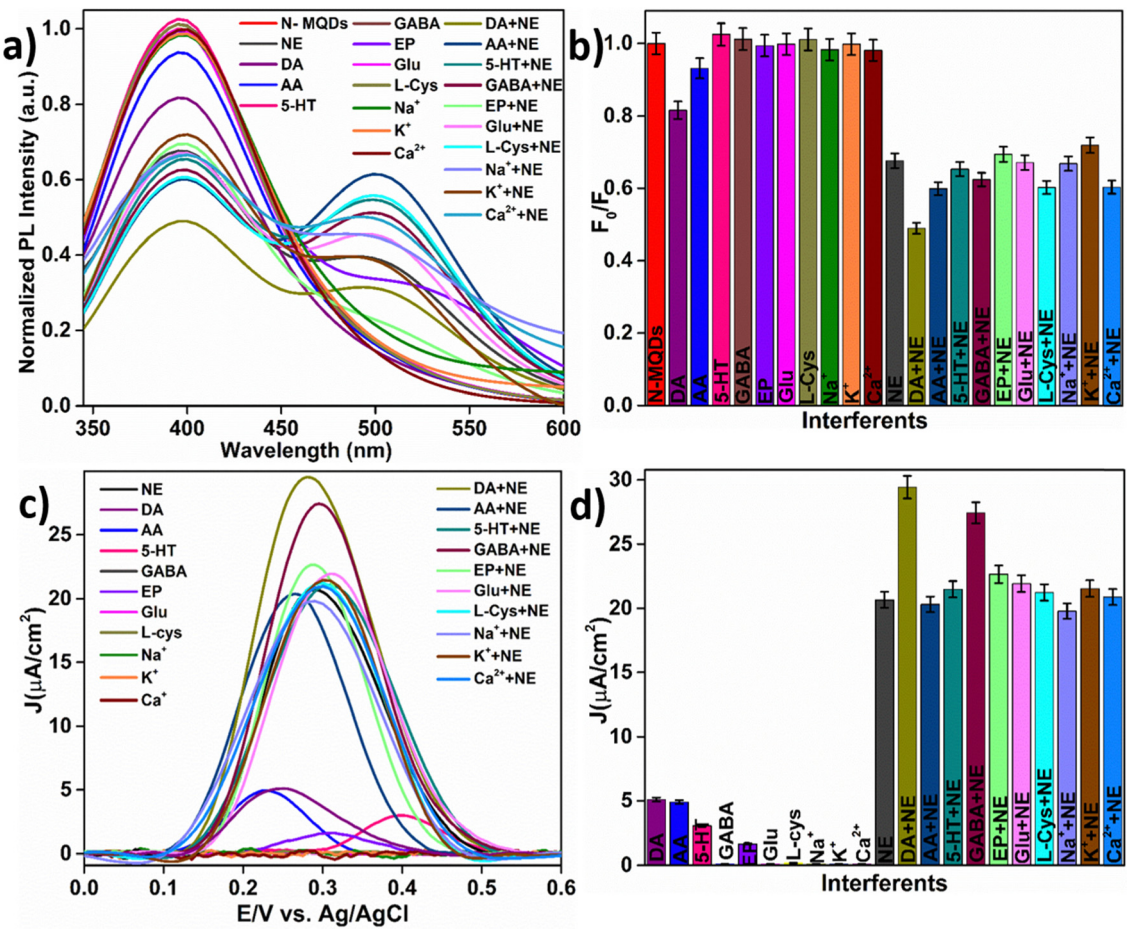

Fig. 7 Specificity of the developed sensor in the presence of interferents using PL spectrum and electrochemical analysis. (a) PL spectrum of N-MQDs in the presence of interfering compounds, (b) corresponding bar chart diagram. (c) DPV analysis of NE detection using a N-MQD modified electrode in the presence of interferents, and (d) corresponding bar chart diagram.

L-ascorbic acid (AA), epinephrine (EP), and metal ions (Na^+, K^+, Ca^{2+}). Fluorescence and DPV analyses were conducted to determine the specificity of the sensor (Fig. 7). N-MQDs were tested with and without various interferents, including DA, AA, EP, 5-hydroxytryptamine (5-HT), gamma-aminobutyric acid (GABA), glucose (Glu), L-cysteine (L-Cys), Na^+, K^+, and Ca^{2+}, for the specificity study. A concentration of 250 μM NE was used, with all interferent samples at the same concentration (Fig. 7a). Among them, 5-HT showed 1% fluorescence enhancement, whereas all the others showed a fluorescence quenching of 1%, except for AA, NE, and DA. Because of their similar structures, AA (7%), DA (19%), and NE (33%) exhibited fluorescence quenching; however, quinone formation occurred only in NE. No other interferents showed an additional peak at 500 nm, except for NE. In addition, NE showed this additional peak even in the presence of high concentrations of all other sources of interferents, indicating that the N-MQDs specifically detected NE only. This new peak confirms the conversion of NE to NE quinone, and the corresponding fluorescence quenching intensities (F_0/F) are shown in the bar chart (Fig. 7b). DPV was also conducted to assess the specificity of the current study, utilizing a potential range of 0 to 0.6 V, a step potential of 0.05 V, an amplitude of 0.025 V, and a scan rate of 50 mV s^{-1}. Similarly, DPV analysis was performed with N-MQD-modified electrodes in the presence of different interferent (1 μM) samples, both with and without NE (1 μM). DPV analysis showed oxidation peak potentials for DA (0.25 V), AA (0.23 V), 5-HT (0.39 V), EP (0.31 V), and NE (0.29 V), while Glu, L-Cys, GABA, Na^+, Ca^{2+} and, K^+ did not show oxidation peaks, as shown in Fig. 7c. The DA, AA, 5-HT, and EP samples show the <5 μA current (owing to the similar structures) and the peak intensity of NE was three times higher than that of other interferents performed individually. Similarly, different interferents in the presence of NE exhibited almost the same current as that of the pristine NE. The relative oxidation peak currents are shown in the bar chart diagram (Fig. 7d), which confirms that the N-MQD-modified electrode exhibits excellent selectivity toward NE oxidation in the presence of high concentrations of other interferents. Fluorescence and electrochemical experiments show that microwave-synthesized N-MQDs are highly sensitive and selective toward NE, based on NE-to-NE quinone oxidation.[58]

4. Conclusion

This study developed an easy approach for N-MQD synthesis using a microwave-assisted method for the dual-mode (fluorescence and electrochemical) detection of NE in biofluidic environments. HR-TEM and AFM were used to examine the morphology of the N-MQDs. XRD, Raman spectroscopy, IR, and UV-vis spectroscopy were employed to confirm the synthesis of the material. XPS analysis was conducted to investigate the N-MQDs before and after sensing NE and to elucidate the detection mechanisms. As the NE concentration increased from 0.1 to 500 μM in the N-MQDs, fluorescence quenching occurred owing to the conversion of NE to NE quinone *via* FRET, resulting in the appearance of a new peak at 500 nm. Both PBS and serum samples were utilized for practical applications, and an LOD of 37 and 40 nM was achieved respectively. UV-vis spectra were recorded at different concentrations of NE to the N-MQDs, and a color change was observed, both visually and under UV light. A smartphone-integrated sensor array system was used for POC analysis with a response time of 5 min and measures the RGB color changes. DPV studies were performed for the electrochemical detection of NE in both PBS and the serum samples, the LOD was calculated to be 54 and 33 nM, respectively. The synthesized N-MQDs were highly selective for NE oxidation and were easily applicable for real-time analyses in integrated smartphone applications. In the future, N-MQD-based devices will be fabricated using printed circuit boards for specific neurotransmitter detection, which will apply to next-generation POC analyses.

Author contributions

Murugesan Chandran: conceptualization, methodology, writing – original draft, writing – review & editing, formal analysis, and validation. Gayathri Chellasamy: formal analysis, and validation. Mekala Veerapandian: formal analysis, and validation. Barkavi Dhanasekaran: formal analysis, and validation. Saravanan Govindaraju: supervision, investigation, writing – review & editing and validation. Yun Kyusik: project administration, writing – review & editing, funding acquisition, and supervision.

Data availability

The data supporting this article have been included as part of the ESI.†

Conflicts of interest

There are no conflicts to declare.

Acknowledgements

This research was supported by the Basic Science Research Program through the National Research Foundation of Korea (NRF) funded by the Ministry of Education (2021R1A6A1A03038996). This work was supported by the Gachon University research fund of 2024 (GCU-202403950001).

Notes and references

1 S. K. Arumugasamy, G. Chellasamy, S. Gopi, S. Govindaraju and K. Yun, *TrAC, Trends Anal. Chem.*, 2020, **123**, 115766.
2 T. M. Godoy-Reyes, A. M. Costero, P. Gava, R. Martínez-Máñez and F. Sancenon, *ACS Appl. Nano Mater.*, 2019, **2**, 1367–1373.

3 D. Ji, Z. Shi, Z. Liu, S. S. Low, J. Zhu, T. Zhang, Z. Chen, X. Yu, Y. Lu, D. Lu and Q. Liu, *Smart Mater. Med.*, 2020, **1**, 1–9.
4 L. Liu, Q. Li, N. Li, J. Ling, R. Liu, Y. Wang, L. Sun, X. H. Chen and K. Bi, *J. Sep. Sci.*, 2011, **34**, 1198–1204.
5 T. Kanamori, T. Funatsu and M. Tsunoda, *Analyst*, 2016, **141**, 2568–2573.
6 A. Naccarato, E. Gionfriddo, G. Sindona and A. Tagarelli, *Anal. Chim. Acta*, 2014, **810**, 17–24.
7 Y. M. Liu, J. T. Cao, Y. L. Zheng and Y. H. Chen, *J. Sep. Sci.*, 2008, **31**, 2463–2469.
8 S. E. Son, E. Ko, V. K. Tran, W. Hur, H. Choi, H. B. Lee, Y. Park and G. H. Seong, *ChemElectroChem*, 2019, **6**, 4666–4673.
9 X. Chen, L. Zhou, Z. Guo and Q. Song, *Mater. Adv.*, 2024, **5**, 1332–1339.
10 N. Zhou, C. Yin, Y. Yue, Y. Zhang, F. Cheng and F. Huo, *Chem. Commun.*, 2022, **58**, 2999–3002.
11 Y. Zhang, W. Ren, Y. Z. Fan, J. X. Dong, H. Q. Luo and N. B. Li, *Anal. Bioanal. Chem.*, 2019, **411**, 3081–3089.
12 F. N. Wu, J. Zhu, G. J. Weng, J. J. Li, X. W. Chen and J. W. Zhao, *Sens. Actuators, B*, 2023, **379**, 133297.
13 D. F. D. Queiroz, T. R. D. L. Dadamos, S. A. S. Machado and M. A. U. Martines, *J. Sens.*, 2018, **18**, 1223.
14 A. Fajardo, D. Tapia, J. Pizarro, R. Segura and P. Jara, *J. Appl. Electrochem.*, 2019, **49**, 423–432.
15 T. Rajarathinam, D. Thirumalai, M. Kwon, S. Lee, S. Jayaraman, H. J. Paik, J. Lee and S. C. Chang, *Bioenergetics*, 2022, **146**, 108155.
16 T. Palomäki, S. Chumillas, S. Sainio, V. Protopopova, M. Kauppila, J. Koskinen, V. Climent, J. M. Feliu and T. Laurila, *Diamond Relat. Mater.*, 2015, **59**, 30–39.
17 A. S. Tanwar, R. Parui, R. Garai, M. A. Chanu and P. K. Iyer, *ACS Meas. Sci. Au*, 2021, **2**, 23–30.
18 G. Chellasamy, S. R. Ankireddy, K. N. Lee, S. Govindaraju and K. Yun, *Mater. Today Bio*, 2021, **12**, 100168.
19 Y. Zhang, B. Wang, H. Xiong, W. Wen and N. Cheng, *Microchem. J.*, 2019, **146**, 66–72.
20 F. Wei, Y. Wu, G. Xu, Y. Gao, J. Yang, L. Liu, P. Zhou and Q. Hu, *Analyst*, 2014, **139**, 5785–5792.
21 J. An, Y. Shi, J. Fang, Y. Hu and Y. Liu, *J. Chem. Eng.*, 2021, **425**, 130595.
22 Y. Bai, Y. He, M. Wang and G. Song, *Sens. Actuators, B*, 2022, **357**, 131410.
23 Z. Li, Z. Wang, Y. Nie, P. Wang and Q. Ma, *J. Chem. Eng.*, 2022, **448**, 137636.
24 B. Shao, Z. Liu, G. Zeng, H. Wang, Q. Liang, Q. He, M. Cheng, C. Zhou, L. Jiang and B. Song, *J. Mater. Chem.*, 2020, **8**, 7508–7535.
25 C. Guan, X. Yue, J. Fan and Q. Xiang, *Chin. J. Catal.*, 2022, **43**, 2484–2499.
26 R. K. Singh, R. Kumar, D. P. Singh, R. Savu and S. A. Moshkalev, *Mater. Today Chem.*, 2019, **12**, 282–314.
27 M. Naguib, M. Kurtoglu, V. Presser, J. Lu, J. Niu, M. Heon, L. Hultman, Y. Gogotsi and M. W. Barsoum, *MXenes*, Jenny Stanford Publishing, 2011, pp. 15–29.
28 X. Chen, X. Sun, W. Xu, G. Pan, D. Zhou, J. Zhu, H. Wang, X. Bai, B. Dong and H. Song, *Nanoscale*, 2018, **10**, 1111–1118.
29 X. Wang, X. Zhang, H. Cao and Y. Huang, *J. Mater. Chem. B*, 2020, **8**, 10837–10844.
30 A. Ray, A. Banerjee and A. Dubey, *Int. J. Agric. Environ. Biotechnol.*, 2020, **13**, 423–430.
31 E. Einafshar, N. Einafshar and M. Khazaei, *Top. Curr. Chem.*, 2023, **381**, 27.
32 O. Jha, T. K. Yadav and R. A. Yadav, *Spectrochim. Acta, Part A*, 2017, **173**, 307–317.
33 T. Yadav and V. Mukherjee, *Spectrochim. Acta, Part A*, 2018, **202**, 222–237.
34 R. A. Heacock and L. Marion, *Can. J. Chem.*, 1956, **34**, 1782–1795.
35 A. C. Khot, T. D. Dongale, J. H. Park, A. V. Kesavan and T. G. Kim, *ACS Appl. Mater. Interfaces*, 2021, **1**, 5216–5227.
36 J. Luo, W. Zhang, H. Yuan, C. Jin, L. Zhang, H. Huang, C. Liang, Y. Xia, J. Zhang, Y. Gan and X. Tao, *ACS Nano*, 2017, **11**, 2459–2469.
37 A. A. Emerenciano, R. M. do Nascimento, A. P. C. Barbosa, K. Ran, W. A. Meulenberg and J. Gonzalez-Julian, *Membr. J.*, 2022, **12**, 1025.
38 M. Mustakeem, J. K. El-Demellawi, M. Obaid, F. Ming, H. N. Alshareef and N. Ghaffour, *ACS Appl. Mater. Interfaces*, 2022, **14**, 5265–5274.
39 X. Xu, H. Zhang, Q. Diao, Y. Zhu, G. Yang and B. Ma, *J. Mater. Sci.: Mater. Electron.*, 2020, **31**, 175–181.
40 Y. Sun, S. Li, Y. Zhuang, G. Liu, W. Xing and W. Jing, *J. Membr. Sci.*, 2019, **591**, 117350.
41 J. Halim, K. M. Cook, M. Naguib, P. Eklund, Y. Gogotsi, J. Rosen and M. W. Barsoum, *Appl. Surf. Sci.*, 2016, **362**, 406–417.
42 T. Y. Lee, C. Y. Lee and H. T. Chiu, *ACS Omega*, 2018, **3**, 10225–10232.
43 A. Saha, S. K. Basiruddin, S. C. Ray, S. S. Roy and N. R. Jana, *Nanoscale*, 2010, **2**, 2777–2782.
44 D. Marton, K. J. Boyd, A. H. Al-Bayati, S. S. Todorov and J. W. Rabalais, *Phys. Rev. Lett.*, 1994, **73**, 118.
45 V. Natu, M. Benchakar, C. Canaff, A. Habrioux, S. Celerier and M. W. Barsoum, *Matter*, 2021, **4**, 1224–1251.
46 S. Reiche, R. Blume, X. C. Zhao, D. Su, E. Kunkes, M. Behrens and R. Schlögl, *Carbon*, 2014, **77**, 175–183.
47 B. Yu, X. Wang, X. Qian, W. Xing, H. Yang, L. Ma, Y. Lin, S. Jiang, L. Song, Y. Hu and S. Lo, *RSC Adv.*, 2014, **4**, 31782–31794.
48 Q. Gao, T. Li, C. Liu, J. Sun, Y. Liu, L. Hou and C. Yuan, *Carb. Neutrality*, 2023, **2**, 18.
49 A. Amiri, Y. Chen, C. B. Teng and M. Naraghi, *Energy Storage Mater.*, 2020, **25**, 731–739.
50 H. J. Kim, I. S. Bae, S. J. Cho, J. H. Boo, B. C. Lee, J. Heo, I. Chung and B. Hong, *Nanoscale Res. Lett.*, 2012, **7**, 1–7.
51 M. Quan, D. Sanchez, M. F. Wasylkiw and D. K. Smith, *J. Am. Chem. Soc.*, 2007, **129**, 12847–12856.
52 Y. Fu, L. Huang, S. Zhao, X. Xing, M. Lan and X. Song, *Spectrochim. Acta, Part A*, 2021, **246**, 118947.
53 Y. Guo, M. Chen, T. Yang and J. Wang, *Chemosensors*, 2023, **11**, 431.

54 A. RosináJose and K. GirishaKumar, *Anal. Methods*, 2016, **8**, 5801–5805.
55 M. Chandran, G. Chellasamy, M. Veerapandian, B. Dhanasekaran, S. K. Arumugasamy, S. Govindaraju and K. Yun, *J. Colloid Interface Sci.*, 2024, **660**, 412–422.
56 M. Jayakumar, C. Murugesan, C. Andrew, K. Natarajan and R. Sekar, *J. Electrochem. Soc.*, 2022, **169**, 032510.
57 R. Mostafazadeh, Y. Hamidian, N. Erk and E. N. Dragoi, *Carbon Lett.*, 2023, **33**, 1827–1837.
58 S. Baluta, A. Lesiak and J. Cabaj, *Sensors*, 2020, **20**, 4567.